Linear mountain drag and averaged pseudo-momentum flux profiles in the presence of trapped lee waves

By FRANÇOIS LOTT, *Laboratoire de Météorologie Dynamique du CNRS, UPMC Paris 6, case courrier 99, 4 Place Jussieu, 75252 Paris Cedex 05, France*

ABSTRACT

The linear mountain drag in the presence of trapped lee waves is calculated using a two-dimensional linear anelastic model. In many cases, it is shown that the drag is affected by the wave refraction index aloft, but remains well predicted by the drag due to hydrostatic freely propagating mountain waves. In contrary, the vertical profile of the waves' Reynolds stress is very sensitive to the mean flow variation, and often decays with altitude in the steady case and in the absence of dissipation. This apparent contradiction with the conventional Eliassen-Palm relation is simply related to the non-zonal, non-periodic geometry of the domain in which the momentum budget is calculated and to the presence of trapped lee-waves. In this context, the spatial average of the pseudo-momentum conservation equation shows that the wave drag at the ground is equal to the wave pseudo-momentum entering in the domain through its upper and leeward boundaries. In the presence of trapped lee-waves, the amount of pseudo-momentum entering through the leeward boundary represents a significant part of the drag, and explains the difference between the Reynolds stress and the surface drag. In this case, the large-scale flow does not need to be modified inside the physical domain, because the entering pseudo-momentum equals the entering momentum transported by the waves across the domain boundaries. It is suggested that conventional gravity wave drag schemes can easily represent the trapped waves by altering the large scale momentum at low level, when the waves are dissipated.

1. Introduction

The parameterization of mountain gravity wave drag in weather forecasting and climate models significantly improves their performance (Boer et al., 1984; Palmer et al., 1986). In most parameterization schemes, it is assumed that the wave Reynolds stress is constant with altitude, when the background mean wind $U(z)$ has a constant sign, in the absence of dissipation and in the steady case (Eliassen and Palm, 1961). Nevertheless, when the flow varies with altitude, some waves can be trapped at low atmospheric levels and cannot transport momentum far aloft (Scorer, 1949). In this case, the structure of the wave field

E-mail: flott@lmd.jussieu.fr

downstream of the ridge is controlled by the modes that exist in the flow in the presence of a flat ground (Corby and Wallington, 1956; Brown, 1983; Shutts et al., 1994). To determine if those waves are important for the climate, one can compare the drag due to the trapped waves to the drag due to the vertically propagating waves which are parameterized in General Circulation Models. In this context, Wurtele et al. (1987) and Keller (1994) have shown in a few examples where the incident wind varies with height that the drag is essentially controlled by the values of the incident wind and of the buoyancy frequency at the ground. In contrast, the vertical profile of the wave Reynolds stress is very sensitive to the vertical variations of the incident flow, and this is related to the presence of low level trapped waves. These

studies suggest that in some circumstances, the linear mountain drag is close to the freely propagating hydrostatic wave drag, while a significant fraction of the waves emitted are trapped. It is noteworthy that this behavior is consistent with the observations. Indeed, the PYREX and ALPEX campaigns have shown that their are always pronounced differences between the mountain pressure drag measured at the ground and the Reynolds stress measured by airplanes above the mountain peaks (Bougeault et al., 1993; Davies and Phillips, 1985; Hoinka, 1986): the pressure drag is often close to the drag due to freely propagating gravity waves (Bessemoulin et al., 1993), but it is typically one order of magnitude larger then the Reynolds stress. Although this difference can be due to nonlinear three-dimensional effects (Miranda and James, 1992; Schär and Durran, 1996), according to Durran (1986), it is also plausible that the presence of trapped lee waves partly explains it.

When there are trapped waves, the fact that the Reynolds stress decays with altitude does not necessarily mean that the waves are dissipated or unsteady, in contrast to the situation where the disturbance vanishes at the horizontal boundaries of the domain where the momentum budget is made. This apparent contradiction to the conventional Eliassen and Palm (1961) theorem is due to the facts that the Reynolds stress is linked to the vertical component of the pseudo-momentum flux (Scinocca and Shepherd, 1992), and that the trapped waves transport a significant amount of pseudo-momentum horizontally. Furthermore, in the steady undissipated case, the fact that the addition of the pseudo-momentum fluxes across the upward and leeward boundaries of a given domain equals the drag follows from the integration of the pseudo-momentum conservation equations (Scinocca and Shepherd, 1992), and from the fact that the pseudo-momentum fluxes through the ground equals the drag (Andrews and McIntyre, 1978; Durran, 1995b). These different results illustrate how the trapped waves break the relationship between the Reynolds stress and the drag, but they do not show directly if the same steady waves alone can close the momentum budget. Indeed, even for small disturbances, the relationship between the pseudo-momentum fluxes and the momentum fluxes are not obvious when the domain is not periodic and in the

anelastic approximation (Scinocca and Shepherd, 1992). As a consequence, it seems usefull to verify that the momentum and the pseudo-momentum budgets are consistent in the weakly nonlinear steady undissipated case for arbitrary flow profile and domain size. Such a verification also gives further justifications to this work, in the sense that the momentum balance can be closed to the lowest order by the waves described to the lowest-order by a linear model.

The first objective of this paper is to analyze more systematically the result of Wurtele et al. (1987) that the wave drag in the presence of trapped lee waves is not much affected by the wave refraction index aloft. The second objective of this paper is to determine whether the linear hydrostatic drag due to freely propagating gravity waves is a good approximation to the drag when significant non-hydrostatic effects occur aloft. The third objective of this paper is to analyze the vertical profiles of the wave Reynolds stress and to interpret their decay with altitude, in the steady case and in the absence of dissipation, by making pseudo-momentum budgets. In this context, it is also checked that the pseudo-momentum fluxes evaluated with the linear model are also the fluxes of momentum related to the lee waves which are calculated with the linear model to the first-order in the forcing amplitude. In Section 2, the basic equations, the linear model and the different set of numerical experiments are presented. The sensitivity of the mountain drag and of the Reynolds stress profiles to the non-dimensional parameters that characterize wave propagation aloft are presented in Section 3. The pseudo-momentum budget is presented in Section 4. Section 5 discusses the links between the momentum fluxes and the pseudo-momentum fluxes, and the implications for gravity wave drag parameterization schemes.

2. Basic equations and linear model

All the results presented have been obtained using the anelastic approximation (Lipps and Hemler, 1982; Scinocca and Shepherd, 1992). In this approximation, freely propagating gravity waves and trapped mountain waves co-exist, and the equations of motion form a Hamiltonian system. For these purposes, the "strong"

Boussinesq approximation is also convenient (Benjamin, 1986), and it has been verified that all the results obtained are also valid when it is used. The two-dimensional equations that result from the anelastic approximation are

$$\frac{d\boldsymbol{v}}{dt} + \nabla(c_p\theta_o\tilde{\pi}) + c_p\frac{d\pi_o}{dz}\,\tilde{\theta}\boldsymbol{z} = 0, \quad \frac{d\theta}{dt} = 0,$$

$$\nabla\cdot(\rho_o\boldsymbol{v}) = 0. \qquad (1)$$

In this system, the Exner pressure and the potential temperature have been written

$$\pi = \left(\frac{p}{p_r}\right)^\kappa = \pi_0(z) + \tilde{\pi}(x, z, t),$$

$$\theta = T\pi^{-1} = \theta_0(z) + \tilde{\theta}(x, z, t), \qquad (2)$$

where the zero subscript refers to the background state, the tildes represent perturbations, p_r is the surface reference pressure and $\kappa = R/c_p$. If one assumes that the background is in hydrostatic balance,

$$c_p\theta_o\frac{d\pi_o}{dz} = -g, \qquad (3)$$

and invokes the ideal gas law $p = \rho RT$, all the background thermodynamics fields are uniquely determined in terms of the profile $\theta_0(z)$, and the buoyancy frequency is given by $N^2(z) = g\theta_{0z}/\theta_0$. Alternatively, the first equation in (1) can be replaced by the vorticity equation:

$$\rho_o\frac{d}{dt}\left(\frac{\omega}{\rho_o}\right) - c_p\frac{d\pi_o}{dz}\frac{\partial\tilde{\theta}}{\partial x} = 0, \qquad (4)$$

where $\omega = \partial_z u - \partial_x w$, and the continuity equation is identically satisfied if we define the mass flux streamfunction ψ,

$$u = \frac{1}{\rho_0}\frac{\partial\psi}{\partial z}, \quad w = -\frac{1}{\rho_0}\frac{\partial\psi}{\partial x}. \qquad (5)$$

The lower boundary condition is

$$w = \frac{d}{dt}h \quad \text{at} \quad z = h(x). \qquad (6)$$

In this framework, the nature of the waves which result from the interaction between a mountain, $z = h(x)$, and the incident flow characterized by the velocity $U(z)$ and by $\theta_0(z)$ depends on the relative amplitude of the 5 scales, $U(0)/N(0)$, l, $H_e(0)$, d, and H. These scales are related to the

vertical wavelength of the hydrostatic gravity waves, the vertical scale of the incident flow change, the compressibility scale $H_e = \rho_0/\rho_{0z}$, the width and the height of the mountain, respectively. The ratios between the last 4 scales and the first scale, define the 4 parameters,

$$L = \frac{N(0)l}{U(0)}, \quad D = \frac{N(0)d}{U(0)}, \quad C = \frac{N(0)H_e(0)}{U(0)},$$

$$H_N = \frac{N(0)H}{U(0)}, \qquad (7)$$

which will be referred to as a non-dimensional vertical scale, a non-dimensional obstacle length, a non-dimensional compressibility scale and a non-dimensional mountain height, respectively. For all the results presented in this paper, it will be assumed that $H_N \ll 1$, so that the mountain height is small compared to the vertical wavelength of the waves, and the linear approximation can be used (Smith, 1979). In this case, the waves forced by the obstacle satisfy the linear equations:

$$(\partial_t + U\partial_x)\omega' - \left(\frac{\Omega}{\rho_0}\right)_z\partial_x\psi' - c_p\frac{d\pi_0}{dz}\partial_x\theta' = 0, \qquad (8)$$

$$(\partial_t + U\partial_x)\theta' - \frac{N^2\theta_0}{g\rho_0}\partial_x\psi' = 0, \qquad (9)$$

$$\psi'(0) = -\rho_0(0)U(0)h(x) \quad \text{at} \quad z = 0, \qquad (10)$$

where the primes replace the tildes to indicate that only the linear part of the total disturbance is considered. Once it is assumed that the wave field amplitude is controlled by H_N, the generation and the refraction of the waves by the incident flow depend very much on the parameters L, C and D. Indeed, in the steady case, one particular harmonic forced at the ground,

$$\psi'(x, z) = \rho_0^{1/2}\mathcal{R}(\hat{\psi}(z)e^{ikx}), \qquad (11)$$

has a vertical structure which is governed by the Taylor Goldstein equation:

$$\hat{\psi}_{zz} + \left(\frac{N^2}{U^2} - \frac{U_{zz} - (\rho_{0z}/\rho_0)U_z}{U} + \frac{\rho_{0zz}}{2\rho_0}\right.$$

$$\left. - \frac{3\rho_{0z}^2}{4\rho_0^2} - k^2\right)\hat{\psi} =$$

$$\hat{\psi}_{zz} + (S(z) - k^2)\,\hat{\psi} = 0, \qquad (12)$$

where $S(z)$ is the Scorer parameter (i.e., the index

of wave refraction). Near the ground, the vertical wavenumber of an harmonic is, $m^2(0) = S(0) - k^2$. For an obstacle with characteristic width d, the horizontal wavenumber of the forced waves are near $k_c = d^{-1}$, and their vertical wavenumbers at the ground are near,

$$m_c^2(0) \approx \frac{N^2(0)}{U(0)^2}(1 + O(L^{-2}) - O(C^{-1}L^{-1})$$
$$- O(C^{-2}) - D^{-2}), \qquad (13)$$

when the incident flow shear is positive and decreases with height. The last 2 terms in eq. (13) show that immediatly aloft the obstacle, most of the modes are evanescent if the density varies rapidly compared to one vertical wavelength of the disturbance ($C^2 < 1$) or (and) if the obstacle length is small compared to one vertical wavelength of the disturbance $D < 1$). The incidence of the parameter L on the nature of the wave field immediatly aloft the ridge is more complex to describe, since for $L = O(1)$, the WKB analysis upon which this discussion is based is not valid. In particular, for small L, the waves turning heights are close to the ground, a configuration that goes against wave emission. In contrast, the $O(L^{-2})$ term in eq. (13) indicate that when L is small, waves emission is favoured.

To systematically investigate the space described by these 3 parameters would result in a very large number of simulations. Nevertheless, in the atmosphere, the compressibility parameter is often large, which makes the wave fields essentially sensitive to L and D. For this reason, in the simulations that follow, the compressibility parameter is changed only when the flow profile is changed and is always large $C \gg 1$, while the parameters L and D vary in ($[1, 8] \times [1, 8]$). This ensures that a significant number of waves are emitted and that the flow varies on scales that are comparable or larger than the typical vertical scale of the disturbances. In most cases presented, non-hydrostatic effects become important aloft because the Scorer parameter decreases with height (Scorer, 1949) and the non dimensional mountain length D controls the amount of harmonics that encounter turning heights, $S(Z_c) = k^2$, where they are reflected downward (Gill, 1982). From (12), it can be predicted that downward reflection will

occur for all the waves whose horizontal wavenumber is larger than $\sqrt{S(\infty)}$. Comparison with the typical wavenumber, k_c, indicates that low-level confinement will occur for most waves if

$$D < \frac{1}{\sqrt{S(\infty)}}\frac{N(0)}{U(0)}.$$

In the following, the ratio

$$\frac{1}{\sqrt{S(\infty)}}\frac{N(0)}{U(0)} \approx 5,$$

and since $D \in [1, 8]$, situations where most waves are trapped and where most waves propagate to $z = \infty$, are considered.

The linear response to the mountain is evaluated using a time-dependent numerical model which is close to the one used by Wurtele et al. (1987) or by Lott and Teitelbaum (1993). It solves the linear eqs. (8) and (9) and has sponge layers at the boundaries to mimic wave propagation at $X = \infty$ and $Z = \infty$. A typical model configuration is displayed on the Fig. 1, and further details are given in the Appendix A. In the simulations that follow, the incident flow is given by,

$$U(z) = U_0 = 10 \text{ms}^{-1} \quad \text{and}$$

$$N^2(z) = N_\infty^2 + (N_0^2 - N_\infty^2)\exp\left(\frac{-z}{l}\right), \qquad (14)$$

where

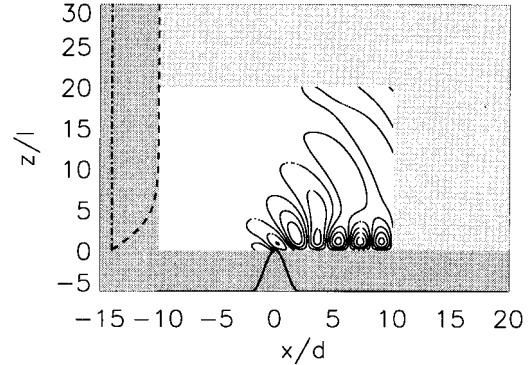$$N_\infty = 0.2N_0 = 10^{-2}s^{-1}$$

Fig. 1. $\psi'/\rho_0^{1/2}$ and model domain description. The light grey areas represent the damping layers. The dark grey areas are outside the model domain. They are displayed to represent the mountain profile (16) (continuous line), and the incident flow (15) (U, long dash; N^2 dot-dash).

or by,

$$U(z) = U_o + (U_\infty - U_0)\tanh\left(\frac{U_0}{U_\infty - U_0}\frac{z}{l}\right) \quad \text{and}$$

$$N(z) = N_0 = 1.8 \cdot 10^{-2}\ \text{s}^{-1}, \tag{15}$$

where
$U_\infty = 5U_0 = 25\ m/s$. The mountain profile is

$$h(x) = \begin{cases} H\cos\left(\dfrac{\pi x}{4d}\right) & \text{if } -2d < x < 2d \\ 0 & \text{otherwise} \end{cases}. \tag{16}$$

In a very idealized way, the incident flow (14) represents a winter continental flow configuration, when the lowermost layers of the atmosphere are very stable because the ground is cold. The incident flow (15) is an idealization of the lower part of the tropospheric jet above the boundary layer. In the parameter space investigated, the total length of the obstacle (16) is $4d$ and typically varies from 1 km to 10 km; the vertical variation of the incident flow l varies from few hundred meters to few kilometers. Although moderate, it is noticeable that these scales are realistic and also that a similar analysis could be done for longer mountains, provided that the low-level wind is larger (the extrema of the incident wind in both profiles (14) and (15) are quite moderate), or that the buoyancy frequency near the ground is smaller (as is often the case in the troposphere).

3. Linear drag and wave's Reynolds stress

To define the drag and the related momentum transfers in the flow the horizontal momentum eq. (1) is integrated over the domain $[h; Z] \times [-X; +X]$, using the lower boundary condition (16):

$$\frac{\partial \overline{\rho_0 u}}{\partial t} + \underbrace{\int_0^Z [\rho_0 u^2 + \rho_0 c_p \theta_0 \tilde{\pi}]_{-X}^{+X}\,\mathrm{d}z}_{[M_x(x,Z)]_{-X}^{+X}}$$

$$+ \underbrace{\int_{-X}^{+X} [\rho_0 uw]^Z\,\mathrm{d}x}_{M_z(X,Z)}$$

$$+ \underbrace{\int_{-X}^{+X} \rho_0 c_p \theta_0 \tilde{\pi}\frac{\mathrm{d}h}{\mathrm{d}x}\,\mathrm{d}x = 0,}_{\mathrm{Dr}} \tag{17}$$

where

$$\overline{\rho_0 u} = \int_{-X}^{+X}\int_{h(x)}^Z \rho_0(z)u(x, z, t)\mathrm{d}z\mathrm{d}x \tag{18}$$

is the mean momentum, $M_x(X, Z)$ is the horizontal momentum flux through a vertical line located at X of height Z, $M_z(X, Z)$ is the vertical flux of momentum across an horizontal line of length $2X$ located at the altitude Z, and Dr is the drag. In the steady case, and to the lowest-order in the forcing amplitude, the drag reduces to the linear wave Reynolds stress evaluated at $Z = 0$:

$$\mathrm{Dr}_{\mathrm{lin}} = -\int_{-X}^{+X} \rho_0 u'w'(x, 0)\mathrm{d}x = -M_z(X, 0); \tag{19}$$

it is independent of X as soon as X exceeds the mountain half length $2d$.

Fig. 2a shows the drag due to linear mountain waves normalized by $\rho_0 N(0)U(0)H^2$, as a function of the two parameters (L, D), for the incident flow profile (14). In the following, the quantity $\mathrm{Dr}_{\mathrm{hyd}} = 1.1\rho_0 N(0)U(0)H^2$ will be called the hydrostatic predictor of the mountain wave drag, $\mathrm{Dr}_{\mathrm{lin}}$. It is the drag due to freely-propagating gravity waves, forced by the mountain (16) in a uniform flow ($U(z) = U(0)$ and $N(z) = N(0)$) for large mountains ($D \gg 1$) and large compressibility scale (i.e., it has been evaluated with the model in the Boussinesq limit $C \gg 1$). Fig. 2a shows that the drag is rather different from the hydrostatic predictor when the incident flow varies rapidly in the vertical direction compared to one typical vertical wavelength of the waves (i.e., for the smallest values of L). For instance, when $L = 1$, the drag is very sensitive to the non-dimensional mountain length D and is often small compared to the hydrostatic predictor. In this case, most of the forced waves become evanescent very close aloft the ridge. Interesting results are found when $L = 2$. In this case, the linear drag is very sensitive to the non-dimensional mountain length D. For instance, it significantly exceeds the hydrostatic predictor when $D = 3, 4, 5$ and 6. This indicates that wave reflection aloft can have a significant feedback influence on the pressure field near the ridge, which in some cases increases the drag. At larger L, the forced waves are also refracted, but this occurs far above the obstacle, so it does not affect the drag as much. Accordingly, the hydrostatic predictor becomes appropriate at large L and when $D > 2$. It only overestimates the drag for all values of L when
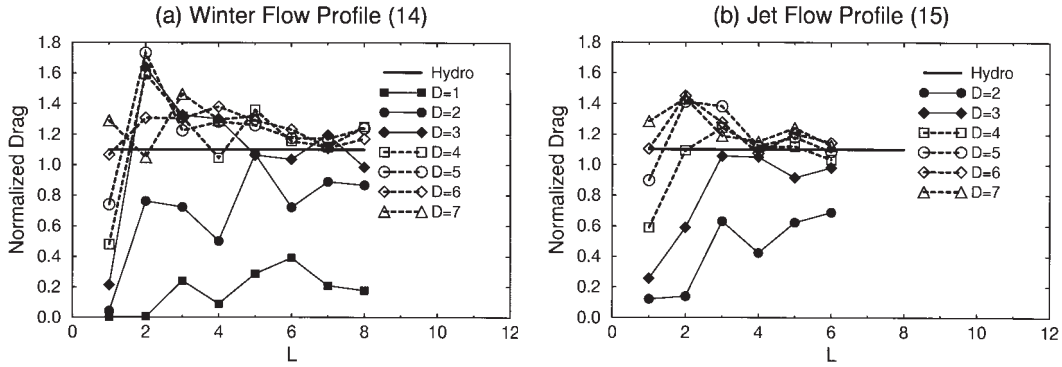
Fig. 2. Wave drag for different values of the parameters L and D, and for the mountain profile (16). Hydro is the drag due to freely-propagating waves in the Boussinesq limit.

$D \approx 1$. Fig. 2b shows similar sensitivity experiments for the incident flow profile (15). Although the dynamical configuration is very different, the dependence of the drag upon the parameters L and D is quite close. The most important difference is that the feedback effect on the drag of the waves reflection when $L = 2$ is not as pronounced as before. This is probably due to the fact that the downstream advection of the waves is faster in this configuration because the incident wind becomes large aloft and the waves reflected downward do not as significantly influence the pressure field near the mountain.

The vertical profiles of the linear wave Reynolds stress,

$$\mathrm{Re}(X, Z) = \int_{-X}^{+X} [\rho_0 u'w']^Z \mathrm{d}x, \qquad (20)$$

evaluated over rather large domains $X \geqslant 10$, is shown in Fig. 3 for two examples with different incident flow profiles, and different values of both L and D. In both cases, the waves Reynolds stress decays with height for all values of the physical domain length, X. When the domain height $Z = 20l$, the Reynolds stress at the top is half the drag in profile (14) when $L = 3$ and $D = 5$, it is 30% of the drag in profile (15) when $L = 2$ and $D = 3$. Although the two examples are different in many respects, the amplitude of the discrepancy between the surface stress and the stress at high level was found to depend only on the non-dimensional mountain length D, which controls the number of modes trapped at low level. Fig. 3b also shows that some distinction can be made between areas where the waves are freely propagating and the

area where they are trapped. It is clear that the effect of wave trapping on the Reynolds stress profiles is noticeable everywhere below the incident wind maximum (i.e., below $z/l \approx 5$). Above the incident wind maximum, the freely propagating waves remains, whose Reynolds stress is constant with altitude. On the other hand, in Fig. 3a, this distinction on the Reynolds stress profile between low and high altitudes is not as clear. This qualitative difference was also found to be related to the mountain width parameter D, not to the incident flow profile or to the vertical scale of the incident flow variation L.

4. Linear drag and averaged pseudo momentum fluxes

The decay with altitude of the waves Reynolds stress is due to the fact that the Reynolds stress (20) is not the only term that contributes to the momentum transfers by the waves. First, it is related to the quadratic part of the vertical flux of momentum (defined in 17),

$$M_z(X, Z) = \int_{-X}^{X} [\rho_0 uw]^Z \mathrm{d}x$$
$$= \int_{-X}^{X} [\rho_0 (U(Z) + \tilde{u})\tilde{w}]^Z \mathrm{d}x, \qquad (21)$$

which contains a non-quadratic term. Secondly, momentum transfers by the waves in the horizontal direction (i.e., $M_x(X, Z) \neq 0$), can occur. Then, to describe the wave propagation and interaction with the large-scale flow, the pseudo-momentum flux diagnostics are better adapted
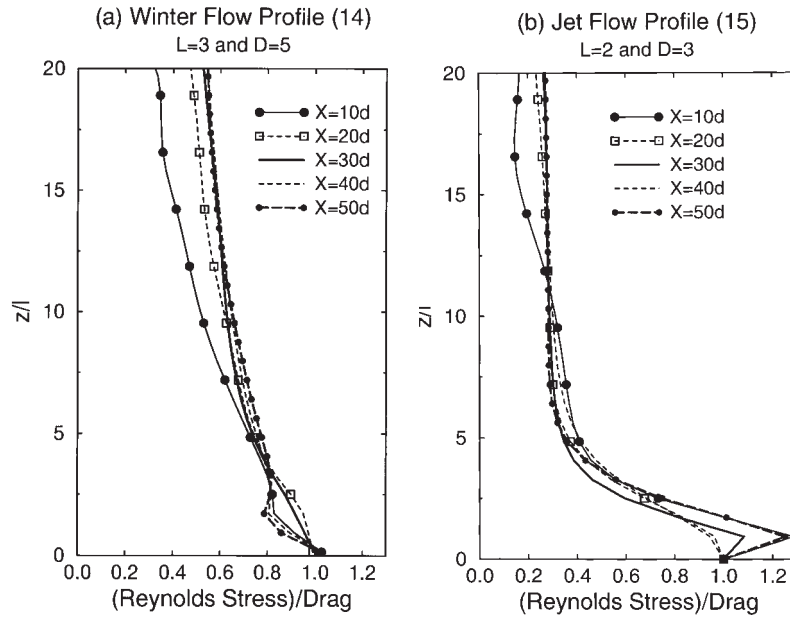
Fig. 3. Vertical profiles of the wave Reynolds stress, Re (X, Z), for different physical domain length X.

(Shepherd, 1990; Scinocca and Shepherd, 1992). In the anelastic approximation, the local form of the pseudo-momentum at the second order in the forcing amplitude is given by:

$$A = \frac{g\rho_0}{\theta_0 N^2}\,\theta'\omega' + \frac{g^2\rho_0}{2\theta_0^2 N^2}\frac{\mathrm{d}}{\mathrm{d}z}\left(\frac{\Omega}{\rho_0}\right)\theta'^2 , \qquad (22)$$

where $\Omega(z)$ is the incident flow vorticity. The pseudo-momentum A satisfies the conservation equation,

$$\frac{\partial A}{\partial t} = -\nabla \cdot \boldsymbol{F}, \qquad (23)$$

in absence of dissipative processes, and the flux $\boldsymbol{F}$ is given by:

$$F_x = \frac{g\rho_0 U}{\theta_0 N^2}\,\theta'\omega' + \frac{g^2\rho_0}{2\theta_0^2 N^2}\left(1 - \frac{\rho_0 U}{N^2}\frac{\mathrm{d}}{\mathrm{d}z}\left(\frac{\Omega}{\rho_0}\right)\right)\theta'^2$$

$$-\frac{1}{2}\left\{\left(\frac{\partial}{\partial x}\frac{\psi'}{\rho_0^{1/2}}\right)^2 - \left(\frac{\partial}{\partial z}\frac{\psi'}{\rho_0^{1/2}}\right)^2\right.$$

$$\left. + \left[\frac{1}{2\rho_0}\frac{\mathrm{d}^2\rho_0}{\mathrm{d}z^2} - \frac{3}{4\rho_0^2}\left(\frac{\mathrm{d}\rho_0}{\mathrm{d}z}\right)^2\right]\frac{\psi'^2}{\rho_0}\right\}, \qquad (24)$$

$$F_z = -\left(\frac{\partial}{\partial x}\frac{\psi'}{\rho_0^{1/2}}\right)\left(\frac{\partial}{\partial z}\frac{\psi'}{\rho_0^{1/2}}\right). \qquad (25)$$

For the following discussion, it is also convenient to define the quantities,

$$P_x(X, Z) = \int_0^Z F_x(X, z)\mathrm{d}z,$$

$$P_z(X, Z) = \int_{-X}^{-X} F_z(x, Z)\mathrm{d}x, \qquad (26)$$

which are the horizontal flux of pseudo-momentum averaged over the vertical and horizontal lines that are used to define the boundaries of the domain. In this framework, the Reynolds stress Re (defined in 20) is quite close to the averaged flux of pseudo-momentum P_z,

$$Re(X, Z) = P_z(X, Z) - \left[\frac{1}{4\rho_0}\frac{\mathrm{d}\rho_0}{\mathrm{d}z}\frac{\psi'^2}{\rho_0}(x, Z)\right]_{-X}^{+X}, \qquad (27)$$

the second term on the rhs of eq. (27) being small when the compressibility scale and X are large (this will be verified later). Then, the integration of the local pseudo-momentum eq. (23) over the domain $[-X, X] \times [0, Z]$ links the surface wave drag to the pseudo-momentum flux across the upward and leeward boundaries of the integration domain in the presence of steady undissipated

waves:

$$-D_{\text{lin}} = P_z(X, 0) = P_z(X, Z) + P_x(X, Z). \qquad (28)$$

To establish (28), the contribution of the pseudo-momentum flux through the upstream boundary is neglected because $P_x(-X, Z)$ was always found to be very small.

Fig. 4, shows the pseudo-momentum flux vector $\textbf{\textit{F}}$ field when the incident flow is uniform. As shown by Scinocca and Peltier (1994), the pseudo-momentum flux is directed downward and the ground is a pseudo-momentum sink. When the buoyancy frequency decreases with height, and for $L = 3$ and $D = 5$, Fig. 5 shows that there are trapped lee-waves that propagate downstream together with some long gravity waves which propagate aloft. The $\textbf{\textit{F}}$ field still shows that the mountain is
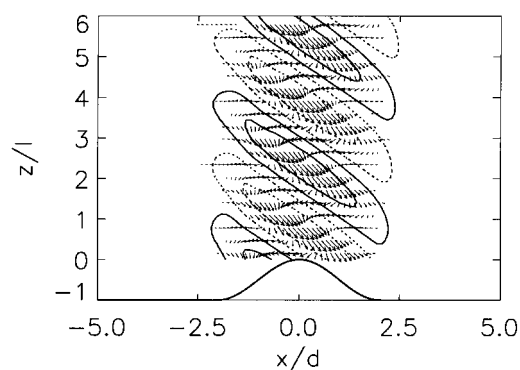

Fig. 4. $\psi'/\rho_0^{1/2}$ and pseudo-momentum fluxes, $\textbf{\textit{F}}$. $\textbf{\textit{F}}$ is plotted every 2 model gridpoints in the both horizontal and vertical directions; uniform flow profile $U = 5$ m/s, $N = 1.8 10^{-2}$ s^{-1}; $L = 2$ and $D = 10$.
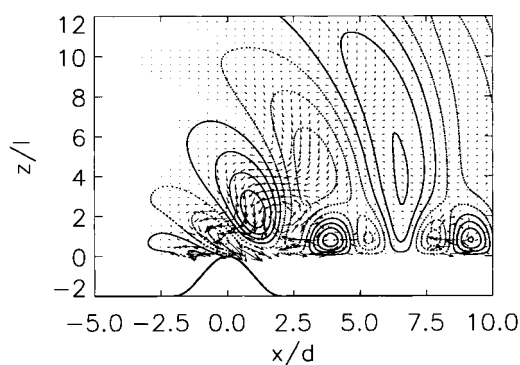
a pseudo-momentum sink, but it now splits into two branches. At high level, the pseudo-momentum flux is essentially oriented downward and is linked to the waves that propagate vertically. The low part of the $\textbf{\textit{F}}$ field has a more complex pattern: the vectors in some places, are oriented horizontally and leeward, in other places, they are oriented vertically and upward. This complex structure arises because the wave field downstream is made up of the superposition of many different interfering wave packets, reflecting several times at the ground and at turning heights. The pseudo-momentum flux vectors are nevertheless predominantly horizontal and oriented toward the mountain, in the lee and at low level. This last property is clearer on Fig. 6 which shows the wave field and pseudo-momentum flux vectors in profile (15) with $L = 2$ and $D = 3$.

The fact that there is a large windward pseudo-momentum flux at low level in both flow configurations, is better indicated on Fig. 7 which represents P_x as a function of the downstream distance X, and for different altitudes, Z. In the lee, P_x is always very significant compared to the drag, and does not decrease with downstream distance for large X (i.e., for $X \geqslant 30d$). As Z increases, and for large X, the amount of pseudo-momentum transported across the leeward boundary tends toward a constant value which represents that part of the mountain drag which is transported horizontally by the lee waves. It represents 45% of the drag when $D = 5$ in profile (15) (Fig. 7a) and 70% of the drag when $D = 3$ in profile (15) (Fig. 7b). A systematic evaluation of the fraction of the drag
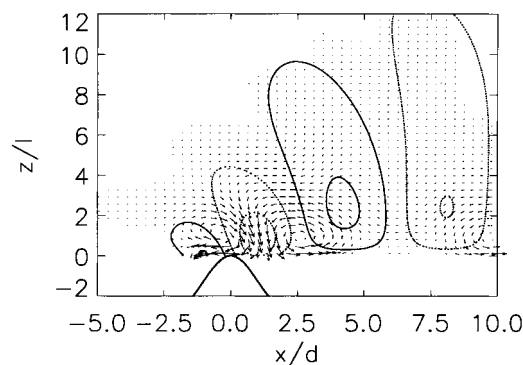

Fig. 5. $\psi'/\rho_0^{1/2}$ and pseudo-momentum fluxes, $\textbf{\textit{F}}$. $\textbf{\textit{F}}$ is plotted every 3 model gridpoints in both horizontal and vertical directions. Flow profile (14), $L = 3$ and $D = 5$.

Fig. 6. $\psi'/\rho_0^{1/2}$ and pseudo-momentum fluxes, $\textbf{\textit{F}}$. $\textbf{\textit{F}}$ is plotted every 3 model gridpoints in both horizontal and vertical directions. Flow profile (15), $L = 2$ and $D = 3$.
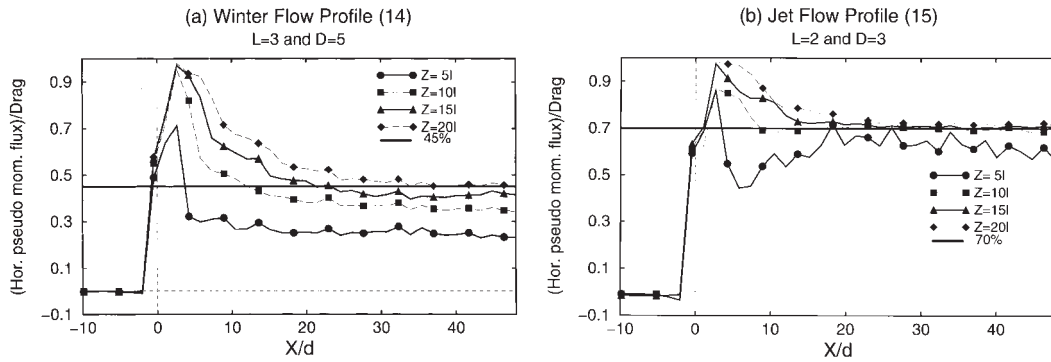
Fig. 7. Horizontal profiles of the pseudo-momentum fluxes through a vertical line, $P_x(X, Z)$, as a function of its horizontal position X and for different line heights Z.

that is transported horizontally by the trapped waves is given in Fig. 8, for a given incident flow but varying the mountain width. It verifies that as long as the parameter

$$D \leqslant 5 \approx \frac{1}{\sqrt{s(\infty)}} \frac{N(0)}{U(0)},$$

more than half of the drag is transported horizontally. For larger values of D, the contribution of the trapped waves to the drag transfer is decreasing. It nevertheless remains significant until $D \approx 10$. Fig. 9 shows the vertical profile of the pseudo-momentum fluxes averaged over the upper and leeward boundaries of the physical domain (28)
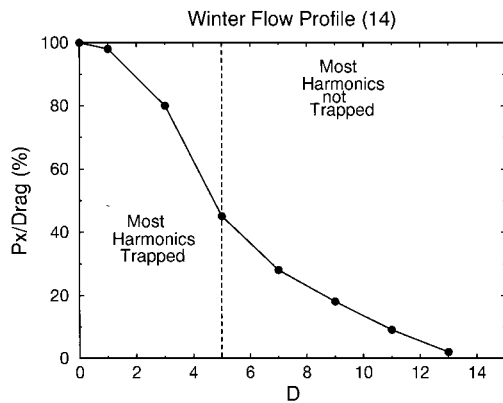

Fig. 8. Fraction of the mountain drag transported horizontally by the trapped waves, and for different values of D. Values shown are evaluated very far upstream: $X/d = 50$ and over a deep domain $Z/l = 20$. For both values, convergence of P_x was reached (it does not change when the domain bounds X and Z increase).

when $X = 20$. It is constant with height, indicating that in the presence of trapped waves, the decay with height of the vertical flux of pseudo-momentum P_z is exactly balanced by an increase of the horizontal flux of pseudo-momentum P_x. The Reynolds stress Re is also plotted on this figure, verifying that it is indeed very close to the vertical flux of pseudo-momentum, P_Z. The fact that the trapped waves transport a finite amount of pseudo-momentum horizontally and that the Reynolds stress decays with altitude independent of the domain length, seems to contradict the results of Keller (1994), who has shown that the Reynolds stress at all altitudes, asymptotes the wave drag, provided that the domain length is long enough. This difference may be related to the fact that the incident flow profiles are different from those used in Keller (1994), so that the harmonics which are trapped at low level in Keller (1994) eventually leak weakly in the stratosphere.

5. Pseudo-momentum fluxes and second-order wave momentum fluxes

As discussed in McIntyre (1980), it is known that pseudo-momentum flux conservation means that there is no torque exerted on the large-scale flow in the Lagrangian context. Nevertheless, when the spatial averages are made over a non-periodic finite domain, the assumptions used to develop the general lagrangian description of wave-mean flow interaction (Andrews and McIntyre, 1978) are not easy to satisfy. In this context, it does not directly follow from the
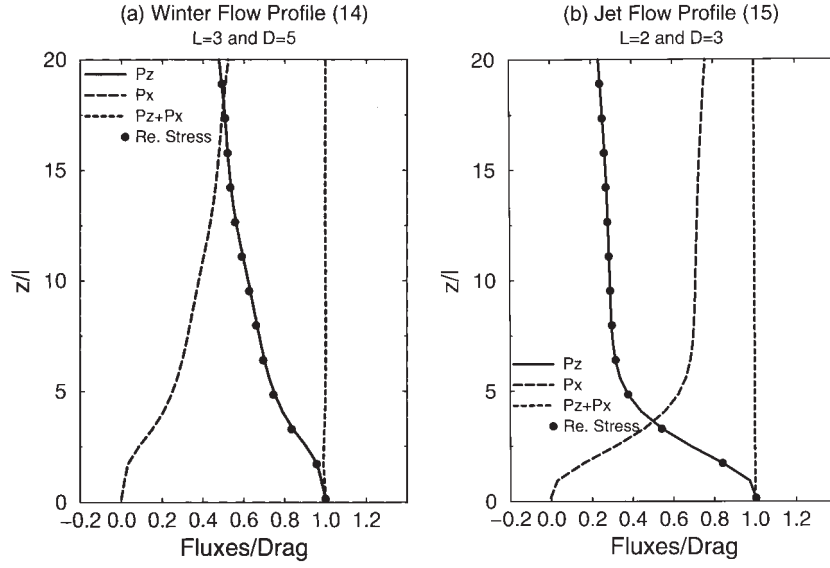
Fig. 9. Vertical profiles of the pseudo-momentum fluxes involved in the steady pseudo-momentum budget. Note that the profiles of P_z and of the Reynolds stress Re are close to one another.

pseudo-momentum conservation budgets that the waves alone can close the momentum budget. In the following, this will be verified, by showing that the momentum flux through the domain boundaries due to the primary steady undissipated waves, is equal to the pseudo-momentum flux through the same boundaries.

To evaluate the momentum fluxes in (17), the fact that the streamfunction, the Bernoulli function and the "Long" function are constant on isentropes,

$$\psi(\theta), \quad \mathscr{B}(\theta) = \frac{u^2}{2} + \frac{w^2}{2} + c_p \theta_0 \pi + c_p \pi_0 \tilde{\theta} + gz,$$

$$\mathscr{L}(\theta) = \frac{\omega}{\rho_0} + c_p \pi_0 \frac{\mathrm{d}\theta}{\mathrm{d}\psi}, \tag{29}$$

is used together with the fact that the disturbances upstream are very small. For instance, the Bernoulli function allows the momentum fluxes, $M = [M_x(x, Z)]_{-X}^{+X} + M_z(X, Z)$ in eq. (17), to be transformed into:

$$M = \int_0^Z \rho_0 \left[\frac{u^2}{2} - \frac{w^2}{2} + \mathscr{B}(\theta) - c_p \pi_0 \tilde{\theta} \right]_{-X}^{+X} \mathrm{d}z$$

$$+ \int_{-X}^{+X} [\rho_0 uw]^Z \mathrm{d}x. \tag{30}$$

Obviously, the largest discrepancy between the

integrands in eq. (30) and the pseudo-momentum fluxes (24) and (25) comes from the non-quadratic terms. To show, nevertheless, that those terms cancel out at first order, it is convenient to split M in two integrals $M_1 + M_2$, where

$$M_1 = \int_0^Z \rho_0 [\mathscr{B}(\theta) - \mathscr{B}(\theta_0) - c_p \pi_0 \tilde{\theta} + U \tilde{u}]^X \mathrm{d}z$$

$$+ \int_{-X}^{+X} [\rho_0 U \tilde{w}]^Z \mathrm{d}x \tag{31}$$

contains non-quadratic terms to lowest order and

$$M_2 = \int_0^Z \rho_0 \left[\frac{\tilde{u}^2}{2} - \frac{\tilde{w}^2}{2} \right]^X \mathrm{d}z + \int_{-X}^{+X} [\rho_0 \tilde{u} \tilde{w}]^Z \mathrm{d}x \tag{32}$$

is quadratic already. To transform M_1, the Bernoulli function is expanded in a Taylor series:

$$\mathscr{B}(\theta) = \mathscr{B}(\theta_0) + \dot{\mathscr{B}}(\theta_0) \tilde{\theta} + \ddot{\mathscr{B}}(\theta_0) \frac{\tilde{\theta}^2}{2} + \dots, \tag{33}$$

where $\mathscr{B}(\theta_0)$ and its derivatives are evaluated upstream and using the inverse function of $\theta_0(z)$ (hereinafter noticed $\mathscr{Z}(\theta)$), and dots represent derivative with respect to θ. Similar developments in $\tilde{\theta}$ of the total streamfunction ψ and of the

"Long" function $\mathscr{L}$, give the relationships,

$$\tilde{\psi} = \rho_0 U \dot{\mathscr{L}} \tilde{\theta} + \ddot{\psi}(\theta_0) \frac{\tilde{\theta}^2}{2} + \dots \quad \text{and}$$

$$\tilde{\omega} = -\frac{g}{\theta_0 U}\left(1 - \frac{\rho_0 U}{N^2}\frac{d}{dz}\left(\frac{\Omega}{\rho_0}\right)\right)\tilde{\theta} + \dots. \quad (34)$$

Combined with eq. (33) they allow to transform M_1 into,

$$M_1 = \int_0^Z \left[\frac{g\rho_0 U}{\theta_0 N^2}\tilde{\omega}\tilde{\theta} \right.$$
$$\left. + \frac{g^2\rho_0}{\theta_0^2 N^2}\left(1 - \frac{\rho_0 U}{N^2}\frac{d}{dz}\left(\frac{\Omega}{\rho_0}\right)\right)\frac{\tilde{\theta}^2}{2}\right]^x dz + \dots (35)$$

Integration of eq. (32) by parts gives,

$$M_2 = \int_0^Z \left[-\frac{1}{2}\left\{\left(\frac{\partial}{\partial x}\frac{\tilde{\psi}}{\rho_0^{1/2}}\right)^2 - \left(\frac{\partial}{\partial z}\frac{\tilde{\psi}}{\rho_0^{1/2}}\right)^2\right.\right.$$
$$\left.\left. + \left[\frac{1}{2\rho_0}\frac{d^2\rho_0}{dz^2} - \frac{3}{4\rho_0^2}\left(\frac{d\rho_0}{dz}\right)^2\right]\frac{\tilde{\psi}^2}{\rho_0}\right\}\right]^x dz$$
$$+ \int_{-X}^{+X}\left[-\left(\frac{\partial}{\partial x}\frac{\tilde{\psi}}{\rho_0^{1/2}}\right)\left(\frac{\partial}{\partial z}\frac{\tilde{\psi}}{\rho_0^{1/2}}\right)\right]^z dx. \quad (36)$$

To the lowest order in the forcing amplitude, one can replace the total disturbance fields (denoted by tildes) by their linear approximation (denoted by primes) in both eqs. (35) and (36). Then, to the second order in the forcing amplitude, the sum of eq. (35) and of the first integral in eq. (36) equals the integrated horizontal flux of pseudo-momentum $P_x(X, Z)$ and the second integral in eq. (36) is the integrated vertical flux of pseudo-momentum $P_Z(X, Z)$. This result, together with the fact that the pseudo-momentum flux averaged over the boundaries of the domain equals the wave drag at the ground, means that the momentum transported by the waves inside the domain exactly balances the drag. In this context, it is important to note that the developments (34) of the streamfunction and of the "long" equation, evaluated to the lowest order in the forcing amplitude, are equivalent to the linear potential temperature, eq. (9), and to the linear vorticity, eq. (8), in the steady case, provided that the waves are very small upstream. It is also important to note that the use of the nonlinear wave solution (29) implies that the only nonlinear rectifications used to evaluate the momentum fluxes can always be calculated locally at success-

ive orders from the linear wave solution and by Taylor expansions of the nonlinear equations (29). These nonlinear rectifications are thus tight to the waves calculated with the linear model, and one can say that the momentum balance is closed by the waves alone: there is no need to introduce any far-field large-scale disturbance.

Fundamentally, the preceding calculation is only a verification that under the usual non-interaction conditions (i.e., when the waves are steady, small and not dissipated), the Eliassen Palm theorem can still apply, even if some constraints on the domain geometry have been relaxed. Nevertheless, a more complete treatment of the problem would be to introduce unsteady effects and dissipation and to try to find connections between the wave momentum fluxes and the wave pseudo-momentum fluxes in this more general context. Although this calculation has not been undertaken, there are a few remarks that can be made and that suggest that if the waves are unsteady or dissipated, the large-scale flow is affected. The simplest case is the unsteady case. For instance, when the wave field has not reached a steady state, the averaged momentum $\overline{\rho_0 u}$ changes, simply because the domain is not periodic for the disturbance itself. Because the averaged momentum $\overline{\rho_0 u}$ is part of what is referred to as the "large"-scale in the momentum budget, the large-scale flow varies in time when the waves field varies in time. Nevertheless, as there is no need to take into account any nonlinear wave-mean flow interaction in this process, this shows that the momentum budgets are not always efficient to separate between the waves and the large-scale flow in the unsteady context.

Now, assume that the flow is steady, but that the low-level waves are dissipated inside the domain far from the boundaries and far from the mountain. The place where the waves are dissipated is a pseudo-momentum source*. There is thus an exchange between that source and the ground, and the pseudo-momentum fluxes through the boundaries are significantly smaller than the surface drag. In this case, as there are no

---

* Sign convention in the pseudo-momentum definition leads to the fact that the mountain which forces the waves appears as a pseudo-momentum sink, while the locations where the waves are absorbed appear as pseudo-momentum sources.

momentum sources or sinks inside the fluid for the total motion (assuming further that there is no friction at the ground), the drag still has to be transported outside the domain. This means that the large-scale flow has to be modified to compensate by a momentum flux deficit, the pseudo-momentum flux convergence, that results from wave dissipation (a detailed analysis of this process is given in Durran (1995a)). To complete this remark, it is also worth noting that to the lowest order, the large-scale flow distortions are of second order in the forcing amplitude. Then, the fluxes of pseudo-momentum related to these large-scale flow distortions will be of third order in the forcing amplitude. This means that to second order in the forcing amplitude, the pseudo-momentum fluxes are only related to the waves and not to the large-scale flow.

These remarks have a consequence for the parameterization of trapped lee-waves in GCM. If one assumes that the trapped lee-waves are attenuated inside a grid box of a large-scale model, one can directly apply the related drag to the large-scale flow at low level.

6. Conclusion

This paper has shown that for two typical flow profiles (which mimic a winter atmospheric flow over land and the lower part of the tropospheric jet), the mountain wave drag is not very sensitive to the wave refraction index aloft. Accordingly, the wave drag can often be predicted using the flow characteristics observed near the ground. The predictor is the drag associated with freely propagating hydrostatic gravity waves in a background flow that is constant with height. This predictor was tested over a very large number of cases by changing the vertical scale of the incident flow variation and the horizontal length of the mountain. This predictor becomes invalid when the mean flow varies rapidly compared to one vertical wavelength of the disturbances forced at the ground (i.e. when $L \leqslant 1$), and when the obstacle is sharp (i.e., when $D \leqslant 1$). Furthermore, in all the cases studied, there were always trapped waves at low level. Accordingly, those waves cannot transport momentum upward and the Reynolds stress always decays with height in the steady inviscid case. In many cases, the vertical profiles of the

Reynolds stress behave as observed by airplanes during field experiments: a sharp decay below the jet maximum and a constant stress above (Bougeault et al., 1993). Although this apparently contradicts the Eliassen and Palm (1961) result, the difference is easily explained by making pseudo-momentum budgets. These show that the wave Reynolds stress is essentially related to the vertical flux of pseudo-momentum averaged over the upper boundary of the physical domain. Its decay with altitude is simply balanced by a horizontal flux of pseudo-momentum through the leeward limit of the domain. In most cases, this horizontal flux of pseudo-momentum, is significant compared to the wave drag and tends to a constant value in the steady case when the downstream distance and the domain height become very large. It has also been verified that to second order in the forcing amplitude, the averaged pseudo-momentum fluxes are equal to the wave momentum fluxes. This means that in the steady inviscid case, the momentum that is taken to the earth is entirely carried inside the physical domain by the waves. Consequently the large-scale flow does not need to be modified, because the exact balance between the mountain drag and the momentum fluxes is maintained by the waves only.

These results justify the introduction of low-level gravity waves in different gravity wave drag parameterization schemes (Miller et al., 1989; Lott and Miller, 1997). In essence, the low-level wave drag referred to in the present work is very different from the blocked flow drag (Lott and Miller, 1997) that has been recently introduced in the ECMWF model, and that decelerates the mean flow at model levels which do not pass over the sub-grid scale mountains. Although the introduction of a low-level gravity wave drag is also justified by the fact that mountain waves break at low level in the non-linear context, another possibility is that trapped waves are dissipated at low level. In this case, a force is applied to the large-scale flow to compensate for a large-scale momentum deficit; the wave pseudo-momentum fluxes convergence due to the dissipation. These effects can easily be included in a GCM gravity wave drag parameterization scheme, since it has been shown in the present paper that the drag is often well predicted by the hydrostatic gravity wave drag, calculated using the low-level flow characteristics.

7. Acknowledgements

8. Appendix A

The model solves eqs (8) and (9) in spectral space in the horizontal direction and in finite-differences in the vertical direction. In time, the evolution equations are solved by one Euler step, followed by successive leapfrog steps. After each time step, an Asselin filter is applied. Furthermore, some linear dampings are introduced (Rayleigh friction and Newtownian cooling) on the right-hand side of eqs. (8) and (9) to define sponge layers at the leeward and upward boundaries of the model domain. The width of the leeward sponge layer is equal to $10d$, where d is a quarter of the mountain length. At the upper boundary, the damping layer has a depth of $10l$, where l scales the vertical variations of the incident flow. The amplitude of the dampings was then adjusted to minimize backward wave reflections and to maximize absorption. These damping layers are very important because they simulate wave propagation at $X = \infty$ and $Z = \infty$. A typical model configuration is displayed in Fig. 1. In most cases, the model resolution is $\Delta x/d = \Delta z/l = 0.1$ with time step $\Delta t = \Delta x/(4U_\infty)$. It is sometimes more accurate to verify model convergence when the wave field has small patterns that need higher resolution to be properly solved. Each simulation begins with an initiation period that lasts $T_{ini} = 10d/U_0$, during which the incident wind increases toward a constant profile.

REFERENCES

Andrews, D. G. and McIntyre, M. E. 1978. On wave-action and its relatives. *J. Fluid Mechanics* **89**, 647–664.

Benjamin, T. 1986. On the Boussinesq model for two-dimensional wave motions in heterogeneous fluids. *J. Fluid Mechanics* **165**, 445–474.

Bessemoulin, P., Bougeault, A., Genoves, P., Jansa Clar, A. and Puech, D. 1993. Mountain pressure drag during PYREX, *Beitr. Phys. Amosph.* **66**, 305–325.

Boer, G. J., McFarlane, N. A., Laprise, R., Henderson, J. D. and Blanchet, J. P. 1984. The canadian climate centre spectral atmospheric general circulation model. *Atmos.-Ocean* **22**, 397–429.

Bougeault, P., Jansa, A., Attie, J., Beau, I., Benech, B., Benoit, R., Bessemoulin, P., Caccia, J., Campins, J., Carrissimo, B., Champeaux, J., Crochet, M., Druilhet, A., Durand, P.. Elkhafi, A., Flamant, P., Genoves, A., Georgelin, M., Hoinka, K., Klaus, V., Koffi, E., Kotroni, V., Mazaudier, V., Pelon, J., Petitdidier, M., Pointin, Y., Puech, D., Richard, E., Satomura, T., Stein, J. and Tannhauser, D. 1993. The atmospheric momentum budget over a major mountain range: first results of the PYREX field program. *Annales Geophysicae* **11**, 395–418.

Brown, P. R. 1983. Aircraft measurements of mountain waves and their associated flux over the british isles. *Q. J. Roy. Meteorol. Soc.* **109**, 849–866.

Corby, G. A. and Wallington, C. E. 1956. Air flow over mountains: the lee-waves amplitude. *Q. J. Roy. Meteorol. Soc.* **82**, 266–274.

Davies, H. C. and Phillips, P. D. 1985. Mountain drag along the gotthard section during ALPEX. *J. Atmos. Sci.* **42**, 2093–2109.

Durran, D. R. 1986. Another look at downslope winds. Part 1: The development of analogs to supercritical flow in an infinitely deep, continuously stratified fluid. *J. Atmos. Sci.* **43**, 2527–2543.

Durran, D. R. 1995a. Do breaking mountain waves decelerate the local mean flow. *J. Atmos. Sci.* **52**, 4010–4032.

Durran, D. R. 1995b. Pseudo momentum diagnostics for two-dimensional stratified compressible flow. *J. Atmos. Sci.* **52**, 3997–4009.

Eliassen, A. and Palm, E. 1961. On the transfer of energy in stationary mountain waves. *Geophys. Norv.* **22**, 1–23.

Gill, A. E. 1982. *Atmosphere-ocean dynamics*, Academic Press.

Hoinka, K. P. 1986. Observational studies of mountain generated momentum fluxes. In: *ECMWF seminar/ workshop on observation, theory and modelling of orographic effects*, vol. 1, pp. 137–166.

Keller, T. L. 1994. Implications of the hydrostatic assumption on atmospheric gravity waves. *J. Atmos. Sci.* **51**, 1915–1929.

Lipps, F. B. and Hemler, R. S. 1982. A scale analysis of deep moist convection and some related numerical calculations, *J. Atmos. Sci.* **39**, 2192–2210.

Lott, F. and Miller, M. 1997. A new subgrid scale orographic drag parameterization; its testing in the ECMWF model. *Q. J. Roy. Meteorol. Soc.* **123**, 101–127.

Lott, F. and Teitelbaum, H. 1993. Topographic waves generated by a transient wind. *J. Atmos. Sci.* **50**, 2607–2624.

McIntyre, M. 1980. An introduction to the generalized Lagrangian-mean description of wave, mean-flow interaction. *Pageoph.* **118**, 152–176.

Miller, M. J., Palmer, T. N. and Swinbank, R. 1989. Parametrization and influence of subgridscale orography in general circulation and numerical weather prediction models. *Meteorology and Atmospheric Physics* **40**, 84–109.

Miranda, P. M. A. and James, I. A. 1992. Non-linear three dimensional effects on gravity-wave drag: splitting flow and breaking waves. *Q. J. Roy. Meteorol. Soc.* **118**, 1057–1081.

Palmer, T. N., Shutts, G. J. and Swinbank, R. 1986. Alleviation of systematic westerly bias in general circulation and numerical weather prediction models through an orographic gravity wave drag parametrization. *Q. J. Roy. Meteorol. Soc.* **112**, 2056–2066.

Schär, C. and Durran, D. R. 1996. Vortex formation and vortex shedding in continuously stratified flows past isolated topography. *J. Atmos. Sci.* **54**, 534–554.

Scinocca, J. and Peltier, W. R. 1994. Finite amplitude wave activity diagnostics for {L}ong's stationary solution. *J. Atmos. Sci.* **51**, 613–622.

Scinocca, J. F. and Shepherd, T. G. 1992. Nonlinear wave-activity conservation laws and Hamiltonian structure for the two dimensional anelastic equations, *J. Atmos. Sci.* **49**, 5–27.

Scorer, R. 1949. Theory of waves in the lee of mountains. *Q. J. Roy. Meteorol. Soc.* **75**, 41–56.

Shepherd, T. G. 1990. Symmetries, conservation laws and hamiltonian structure in geophysical fluid dynamics. *Advances in Geophysics* **32**, 287–338.

Shutts, G., Healey, P. and Mobbs, S. 1994., A multiple sounding technique for the study of gravity waves. *Q. J. Roy. Meteorol. Soc.* **120**, 59–77.

Smith, R. B. 1979. The influence of mountains on the atmosphere. *Advances in Geophysics* **21**, 87–230.

Wurtele, M. G., Sharman, R. D. and Keller, T. L. 1987. Analysis and simulations of a troposphere-stratosphere gravity wave model. Part 1. *J. Atmos. Sci.* **44**, 3269–3281.